An accelerated three-dimensional coupled electromagnetic-mechanical model for electromagnetic pulse forming and welding

M. Zhou [a], Z. Li [b]*, H. Assadi [a]*, I. Chang [a], C. Barbatti [b,c]

[a] Brunel Centre for Advanced Solidification Technology (BCAST), Brunel University London, UK

[b] Constellium University Technology Centre, Brunel University London, UK

[c] Constellium Technology Center, Parc Economique Centr'alp, CS 10027, Voreppe, 38341 cedex, France

Abstract

Electromagnetic pulse technology (EMPT) applied engineering practices have seen growing attention and broader industrial demand in response to the rising application of lightweight alloys. As EMPT fabricated components get bigger and more complex, the configuration of computational modelling inevitably needs to expand into the three-dimensional space. Further deployment of EMPT requires a computational model capable of providing insights into the fundamentals of the EMPT applications while meeting the computational thriftiness challenges. In this paper, a reduction coefficient model k is proposed and incorporated into a one-way coupled electromagnetic-mechanical model to simulate the engineering applications of EMPT. The model k, constructed as a decaying exponential function of time, was calibrated and validated by a series of tube compression experiments using EMPT, is able to compute the spatial and temporal reduction effect of the magnetic field in a workpiece. The proposed modelling approach allows an accurate and efficient three-dimensional numerical analysis of the mechanical behaviour in the complex electromagnetic field, substantially accelerated the simulation process compared to the fully coupled electromagnetic-mechanical analysis. The distinctive strain-rate variation observed in the 3D tube compression simulation highlights the potential of EMPT in evaluating material's strain rate sensitivity under complex loading conditions, providing the basis for a new dynamic testing method of alloys.

Keywords: Electromagnetic forming, electromagnetic welding, Three-dimensional electromagnetic-mechanical simulation, Aluminum alloys.

1 Introduction

Electromagnetic pulse technology (EMPT), realised using a capacitor bank and an appropriate tool coil, offers a contact-less process for joining, welding, forming, crimping, and cutting sheet metals and tubes. It exploits the eddy current induced in electrically conductive materials by a single current pulse at a frequency for example of 10 kHz [1].

In the recent decade, electromagnetic pulse forming (EMPF), referred also as EMF, and electromagnetic pulse welding (EMPW) have received growing academic and industrial attention, greatly motivated by the increasing applications of lightweight components, e.g., aluminium [2], magnesium [3], titanium alloys and carbon-fiber-reinforced-polymers [4], in various manufacturing areas. The high-speed nature of the EMF process allows a significant improvement in the formability of aluminium, magnesium, and titanium alloy. Moreover, it minimises the springback effects experienced in the conventional quasistatic metal forming process [5].

The concept of EMPW, typically as considered solid-state welding, was developed in the late 60s and early 70s [6]. The accelerating force provided by the electromagnetic field generates a large impact force that enables metallurgical bonding even between dissimilar metal materials [7], for example, aluminium to stainless steel [8][9], aluminium to carbon steel [10], aluminium to copper [11][12][13], aluminium to magnesium [14]. Despite great advantages of EMPW, a wide-scale industrial application is hindered by the insufficient understanding of the governing mechanism of the process and its associated influencing parameters. EMPW presents significant challenges for empirical investigations for being a speedy transient process that usually completes within a microsecond. The physical observation is often restricted to the applied electrical pulse current profile and the microstructure in the resulting EMPW joints, whereas the critical process parameters, for example, impact velocity and impact angle, remain difficult to measure.

Due to the complex nature of EMPT, numerical analysis has become an essential tool for its future development. Numerical modelling of the EMPF process has been increasingly adopted to assist in more sophisticated forming system design that is required for forming metal into complex shapes [15]. Numerical simulation of the EMPW process has been used to gain insights into developing the thermomechanical field variables at the interface of workpieces that cannot be studied experimentally.

Being a highly coupled multi-physical process, EMPT involves electromagnetic, mechanical mechanics, thermodynamics field. With considerable advancement made in the field of computational simulation, a wide range of multi-physics software such as ANSYS, LS-DYNA, ABAQUS, COMSOL has become available to model such a process with varying degrees of simplifications implemented. A numerical model of EMPT should generally consist of two field domains: the electromagnetic and mechanical domains. The electromagnetic (EM) domain performs the transient electromagnetic analysis, determining the electromagnetic field, the eddy current, and the Lorenz body force, while the mechanical domain conducts the mechanical analysis. For EMPF, the mechanical analysis focuses on providing an accurate prediction of the final deformation of the workpiece; for EMPW, the mechanical analysis is essential for investigating the acceleration, velocity and impact angle while being insightful for understanding the thermomechanical development of materials at the welding interface that is responsible for successful bonding. Thermal simulation can also be included in the mechanical domain.

In the actual EMPT process, the EM domain and the mechanical domain are interactive; however, numerical solutions to the physical model of a completely integrated electromagnetic-thermomechanical model are still computationally challenging. As a simplification, the Lorentz body force can be treated as uniform surface pressure with decaying sinusoid time dependence and decaying exponential spatial distribution from the coil centreline [16]. This type of modelling, consisting of only the mechanical domain, solves the mechanical analysis accurately with pre-determined magnetic pressure loading. However, it requires calibrating the magnetic pressure for every combination of materials and process parameters, which can be particularly difficult for complex geometries [2].

Therefore, the EM field must be included in the numerical modelling to investigate primary process parameters, such as charge energy and airgap, paving the way for system design and optimisation. To model the interacting EM and mechanical domain, one common simplification used in the numerical simulation is the one-way coupling of the two domains, also known as the loose coupling method [17]. In the one-way coupled model, the Lorenz body force calculated in the EM domain is exported to the mechanical domain as the external force for the mechanical analysis, but the mechanical analysis results are not exported to the EM domain. The one-way exportation does not consider the influence of the velocity and the displacement of the workpiece on the transient EM analysis. The loose coupling method is computationally economical; however, existing research [18][19] has found that it is only capable of qualitative comparisons between experimental and predicted deformation. Qiu et al. [17] observed a 50% overestimation of the deformation in their 2D loose coupling model and showed that by applying a crude reduction factor to the coil current input, the overestimation was reduced to 2%. Haiping et al. [20] improved the accuracy of the deformation prediction by 5% by using a 2D sequential coupling simulation in ANSYS. They updated the mesh of the EM model at each time step (40 evenly spaced steps over a total simulation time of 200 μs), based on the mechanical analysis results to account for the impact of geometry changes of the workpiece on the Lorentz body force. Because the geometry changes were realised through manually modifying the mesh, only small deformation is applicable, which would become troublesome for complex-shaped forming. Moreover, the impact of workpiece velocity was still not adequately taken into account. Uhlmann et al. [21] showed better accuracy improvement by including the mechanical domain thermal analysis when using the sequential coupling approach in ANSYS.

Using LS-DYNA, Eplattenier et al. [22] performed a 3D coupled electromagnetic-mechanical simulation where the new geometry computed in the mechanical domain was automatically implemented in the EM field in a Lagrangian way. However, the workpiece velocity could still not be imported to the EM, thus not being considered.

Cao et al. [23] performed a fully coupled electromagnetic-mechanical analysis using COSMOL for the electromagnetic metal sheet forming process, which considered the impact of workpiece deformation and velocity on the EM field. By comparing with experimental results, they demonstrated a noticeable effect of workpiece velocity on the Lorentz body force and the deformation of the workpiece, even though the maximum velocity was lower than 200 m/s. The limitation here is that a 2D axisymmetric EMPF model, the capability of COSMOL to perform a fully coupled 3D electromagnetic-mechanical analysis, has yet to be demonstrated. The volumetric distribution and evolution of the EM field become critical for the EMPW process, where the impact velocity and angle are spatially non-uniform.

In most of the sequentially/fully coupled numerical models that were established for the EMPF process, the velocity was generally lower than expected for the EMPW process. The impact action in the mechanical domain of EMPW presents a significant numerical challenge for a fully coupled simulation approach. Meanwhile, the future development of EMPT demands an accurate, efficient and economical numerical model for its essential role in process system design and optimisation. Unlike the EMPF process, where a two-dimensional model is generally sufficient, the EMPW process greatly needs a three-dimensional model since the spatial distribution of the Lorenz force at the impact surface of the EMPW is critical for successful welding.

To address the above problem, i.e. to find a balance between computational efficiency and reliability, this paper proposes a 3D one-way coupled electromagnetic-mechanical model in conjunction with a time-dependent correction factor compensating for the changes in the magnetic force as a result of dimensional changes. The correction factor, referred to as reduction coefficient *k*, is applied to the input pulse current to account for the encapsulated effect of workpiece deformation and velocity on the EM field. The coefficient *k* is calibrated based on the deformation results of a series of tube compression experiments by EMPT and is proposed as a decaying exponential function of time.

The theoretical background of EMPT is discussed in the next section, focusing on the analytical implications for adopting the one-way coupled simulation approach, providing the foundational basis for the reduction coefficient proposal. Section 3 presents a brief introduction to the proposed reduction coefficient model *k*. The methodology for the tube compression experiment is described in Section 4. Section 5 elaborates the calibration of the coefficient model *k*, using a combination of the experimental results and the numerical investigation. A list of symbols used in this paper is summarised in Table 10 and each symbol is defined as it first appears in the text.

2 Theoretical background

The fundamentals of electromagnetic phenomena as applied to EMPT are well established and summarised by the Maxwell equations. Symbols in bold represent vector quantities.

$$\nabla \times \boldsymbol{E}_{ind} = -\frac{\partial \boldsymbol{B}}{\partial t} \quad \text{Equation 1}$$

$$\nabla \cdot \boldsymbol{B} = 0 \quad \text{Equation 2}$$

$$\nabla \cdot \boldsymbol{E} = \frac{\rho_{tot}}{\epsilon_0} \quad \text{Equation 3}$$

$$\nabla \times \boldsymbol{B} = \mu_0 \left(\boldsymbol{J}_{tot} + \epsilon_0 \frac{\partial \boldsymbol{E}}{\partial t}\right) \quad \text{Equation 4}$$

Where $\boldsymbol{E}_{ind}$ is the induced electric field in the workpiece

$\boldsymbol{B}$ is the magnetic flux density, weber/m^2

$\boldsymbol{E}$ is the electric field intensity, volt/m

$\boldsymbol{J}_{tot}$ the total current density

ρ_{tot} is the total charge density

μ and ϵ are the magnetic permeability and electrical permittivity respectively

μ_0 and ϵ_0 are the magnetic permeability and electrical permittivity of vacuum

Equation 4 shows that an electric current ($\boldsymbol{J}_{tot}$) and a changing electric field ($\frac{\partial \boldsymbol{E}}{\partial t} \neq 0$) produce a circulating magnetic field. Under the low frequency assumption, in the case of EMPT, the second term in Equation 4 can be neglected, and $\boldsymbol{J}_{tot}$ can be simplified to conduction current ($\boldsymbol{J}_{con}$). With the magnetisation of the media is assumed to be of its permeability μ, Equation 4 can be reduced to

$$\nabla \times \boldsymbol{B} = \mu \boldsymbol{J}_{con} \quad \text{Equation 5}$$

In the EMPT process, $\boldsymbol{J}_{con}$ is the conductive current in the coil. The alternating pulse current applied generates an alternating magnetic field ($\frac{\partial \boldsymbol{B}}{\partial t} \neq 0$), which in turn, according to Equation

1, induces an electromotive force (emf), i.e., a circulating electric field ($\boldsymbol{E}_{ind}$) in the nearby flyer workpiece. The $\boldsymbol{E}_{ind}$ drives an electric current (eddy current, $\boldsymbol{J}$) in the nearby workpiece according to Ohmn's law:

$$\boldsymbol{J} = \gamma \boldsymbol{E}_{ind} \qquad \text{Equation 6}$$

Where $\boldsymbol{J}$ is the eddy current density, and γ is the material electrical conductivity.

Subsequently, the workpiece is accelerated outward due to the electromagnetic force (the Lorentz body force F) generated by the cross product of the eddy current density $\boldsymbol{J}$ and the magnetic flux density $\boldsymbol{B}$:

$$\boldsymbol{F} = \boldsymbol{J} \times \boldsymbol{B} \qquad \text{Equation 7}$$

Equation 1 shows the $\boldsymbol{E}_{ind}$ on the workpiece emerges from the variation in the magnetic field experienced by itself during the EMPT process. Rewrite Equation 1 in its integral form using the Stokes' theorem:

$$\oint_{\partial\Sigma} \boldsymbol{E} \cdot d\boldsymbol{l} = -\frac{\boldsymbol{d\Phi_B}}{\boldsymbol{dt}} = -\frac{\mathrm{d}}{\mathrm{d}t}\iint_{\Sigma} \boldsymbol{B} \cdot d\boldsymbol{A} \qquad \text{Equation 8}$$

During the EMPT process, the magnetic flux density $\boldsymbol{B}$ is spatial and time-dependent under the coil current; the area vector A is time-dependent because of the movement, i.e., the change in the position $\boldsymbol{r}$ of the workpiece. Hence applying Leibniz's rule for surfaces moving in three-dimensional space to the integration term in Equation 8:

$$\frac{\mathrm{d}}{\mathrm{d}t}\iint_{\Sigma(t)} \boldsymbol{B}(\boldsymbol{r},t) \cdot d\boldsymbol{A} = \iint_{\Sigma(t)} (\boldsymbol{B_t}(\boldsymbol{r},t) + [\nabla \cdot \boldsymbol{B}(\boldsymbol{r},t)]\boldsymbol{v}) \cdot d\boldsymbol{A} - \oint_{\boldsymbol{\partial\Sigma(t)}} [\boldsymbol{v} \times \boldsymbol{B}(\boldsymbol{r},t)] \cdot d\boldsymbol{l}$$

Equation 9

$\boldsymbol{B}(\boldsymbol{r},t)$ is the magnetic flux density at the spatial position **r** and time t,

The subscript t in $\boldsymbol{B_t}(\boldsymbol{r},t)$ denotes partial differentiation of $\boldsymbol{B}(\boldsymbol{r},t)$ over time t,

r is the position vector,

$\boldsymbol{v}$ is the velocity of the region Σ

Recalling Equation 2 (Gauss's law for magnetism), Equation 9 reduces to

$$\frac{\mathrm{d}}{\mathrm{d}t}\iint_{\Sigma(t)} \boldsymbol{B}(\boldsymbol{r},t) \cdot d\boldsymbol{A} = \iint_{\boldsymbol{\Sigma(t)}} \boldsymbol{B_t}(\boldsymbol{r},t) \cdot \boldsymbol{dA} - \oint_{\boldsymbol{\partial\Sigma(t)}} [\boldsymbol{v} \times \boldsymbol{B}(\boldsymbol{r},t)] \cdot \boldsymbol{dl} \qquad \text{Equation 10}$$

The first term on the right-hand side of Equation 10 corresponds to the induced emf generated by the time-varying coil current, and the second term corresponds to the motional emf generated by the workpiece cutting the magnetic lines as it moves outwards. Combining Equation 8 and Equation 10, we can find the circulating electric field ($\mathbf{E}_{\text{ind}}$) induced in the workpiece using the following Equation:

$$\oint_{\partial\Sigma} \boldsymbol{E_{ind}} \cdot d\boldsymbol{l} = -\iint_{\boldsymbol{\Sigma(t)}} \boldsymbol{B_t}(\boldsymbol{r},t) \cdot \boldsymbol{dA} + \oint_{\boldsymbol{\partial\Sigma(t)}} [\boldsymbol{v} \times \boldsymbol{B}(\boldsymbol{r},t)] \cdot \boldsymbol{dl} \qquad \text{Equation 11}$$

Equation 11 reveals that the induced circulating electric field in the workpiece, the resulted eddy current (Equation 6) and the Lorentz force (Equation 7) are simultaneously affected by the induced emf and the motional emf.

Instead of using Equation 11, the one-way coupling model calculates the Lorentz force using Equation 12, a simplified version of Equation 11. Equation 12 neglects the time dependence in the position vector $\boldsymbol{r}$ by using the value of $\boldsymbol{B}$ at the initial position and disregards the second term of the motional emf.

$$\oint_{\partial\Sigma} \boldsymbol{E_{ind}} \cdot \boldsymbol{dl} = -\iint_{\boldsymbol{\Sigma(t)}} \boldsymbol{B}(\boldsymbol{r_0},\boldsymbol{t})_{\boldsymbol{t}} \cdot \boldsymbol{dA} \qquad \text{Equation 12}$$

Equation 12 provides a definite overestimation of $\boldsymbol{E_{ind}}$. Firstly, using the fixed value of $\boldsymbol{B}$ at the initial position of the workpiece does not account for the attenuation of $\boldsymbol{B}$ due to the increasing distance between the workpiece and the coil. Secondly, the opposite sign between the first term (negative) and the second term (positive) in Equation 11 shows that in the workpiece, the eddy current induced by the coil current is in the opposite direction to the coil current, whereas the eddy current generated by the motional emf is in the same direction to the coil current. As a result, the eddy current by the second term offsets that by the first term. While neglecting the second term, Equation 12 overestimates the eddy current in the workpiece, leading to an overestimation in the Lorentz force.

3 Reduction coefficient (k) model

The theoretical review concluded that the one-way coupling method overestimates the Lorentz force in the workpiece during the EMPT process. A correction to one-way coupled modelling is possible by introducing a reduction coefficient model (k) into Equation 12 to restore the reducing effect of the displacement and velocity. The proposed coefficient should correspondingly consist of two contributors: one accounts for the attenuation of the magnetic flux density ($\boldsymbol{B}$) due to the displacement of the workpiece, the other considers the motional emf resulted from the velocity. In other words, the proposed model *k* is a function of spatial position ($\mathbf{r}$) of the workpiece and the time (t). Considering the position of the workpiece is a function of time ($\mathbf{r}$(t)), in this paper the model *k* is proposed as an evolution function of time, where the spatial reduction effect is implicitly included. The time function *k(t)* could be directly applied to the input coil current (a pulse current time history), allowing the reduction effect to be captured adequately at every time point of the EMPT process.

The acceleration and velocity of the workpiece during the EMPT are incredibly challenging to measure since the whole process completes within microseconds. In this paper, the magnetic field attenuation on the workpiece as it moves away from the coil was deterministically quantified using a series of EM simulations. The changing position of the workpiece was represented by incrementally updating the distance between the workpiece and the coil in each static model of the sequence. At the starting and ending position of the workpiece, where the velocity is zero, the attenuation of $\boldsymbol{B}$ contributes to the total reduction coefficient *k*. Thus, the initial and the final value of *k* could be determined based on the EM simulation results. The contribution from the velocity was quantified by comparing the simulated workpiece deformation profile to the experimental observation. At last, an exponential decay evolution function was proposed to describe the development of *k*, whereby, with the adopted fitting parameters, the best matching of the deformation profile could be obtained. The methodology used for the coefficient model calibration is detailed in the Section 5.

4 Methodology

4.1 Experimental procedure

In order to calibrate the reduction coefficient, a set of tube compression experiments by EMPT were designed and carried out. Aluminium tubes made of AA6063 in T6 condition were deformed by the EMPT system (PS96-16 produced by PST Products GmbH) with various charge energies, operating at a frequency of 12.2kHz. The experimental current flow through the coil was measured using Rogowski coil and used in the numerical simulation. The tube material is commercial AA6063 aluminium alloy with mechanical properties summarised in Table 1. The outer diameter of the tube is 19.05 mm with a wall thickness of 1.22 mm; the length of the tube is 100 mm. For testing, the tube was positioned above the longitudinal centreline of the flat coil, supported by a steel block on the top, as illustrated in Figure 1.

An overview of the selected parameters is summarised in Table 2. The process parameters were selected to achieve a distinguished deformation profile of the tube, without excessive deformation to avoid cracking. Under this experimental configuration, the bottom side of the tube is allowed to deform freely, only subjected to the Lorentz force. Thus, the actual Lorentz force experienced by the tube during the EPMT process can be qualitatively quantified through a study of the deformation profile. The details of the study are discussed in the next section as part of the coefficient calibration.

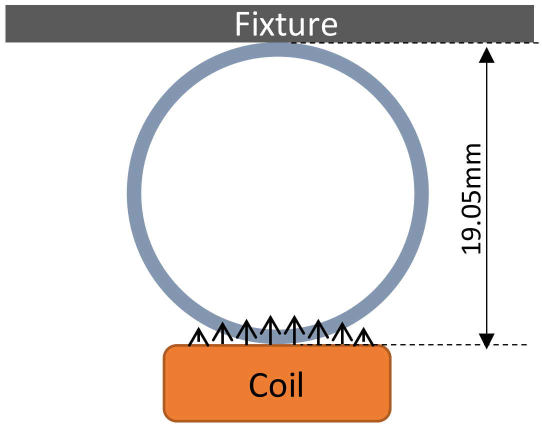

Figure 1: Configuration of the Al tube compression experiment

Table 1: Tensile properties of the examined aluminium samples.

	Alloy	**Temper**	**Yield strength (Rp0.2) [MPa]**	**Tensile strength (Rm) [MPa]**	**Elongation [%]**
Tube	AA6063	T6	170	215	8

Table 2: selected parameters for electromagnetic pulse Al tube compression

Test	**Discharge energy [kJ]**	**Discharge voltage [kV]**	**Max current [kA]**	**Airgap [mm]**	**Frequency [kHz]**
Al tube compression	12	5.4	290.7	-	12.2
	13	5.6	303.0	-	
	14	5.8	315.4	-	
	15	6.0	325.8	-	
	16	6.2	337.0	-	

4.1.1 Characterisation of the deformed tubes

The edge and the middle parts of the deformed tubes were sectioned perpendicularly to its axial direction. Scanned images of these deformed tubes were generated using an Epson Desktop scanners, these scanned images were processed and analysed by ImageJ/Fiji software in order to determine the geometry of each cross section after EMPT process.

4.2 Simulation procedure

A three-dimensional one-way coupled electromagnetic-mechanical model was established in Abaqus. Figure 2 shows a schematic view of the electromagnetic model, where half of the tube and the flat coil are modelled, taking advantage of the structural symmetry about the X-Y plane. The width and height of the coil are 15mm and 5mm, respectively. It should be noted that heating due to plastic deformation and electrical resistance are neglected in this work.

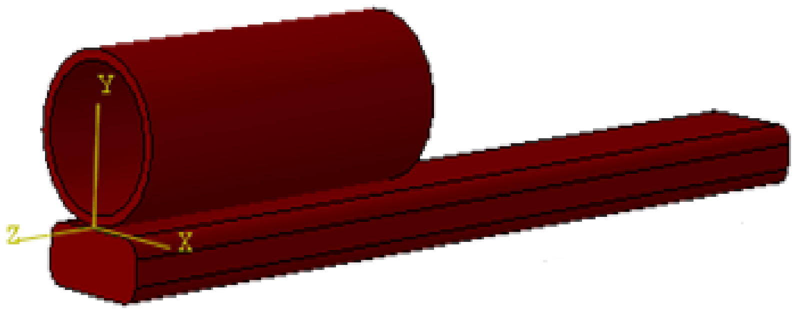

Figure 2: Schematic model view

4.2.1 Coil current profile

A range of pulse current, discharging energy varies from 12-16 kJ, were used in the experiment. Figure 3 shows the measured current profile using Rogowski coil as a function of time. The current density was obtained by dividing the applied current to the coil cross-section area of $1.0157 x 10^{-4}$ m^2. The current profile shows that about 80% of the total stored energy was discharged in the first cycle, and about 95% was discharged after three cycles.

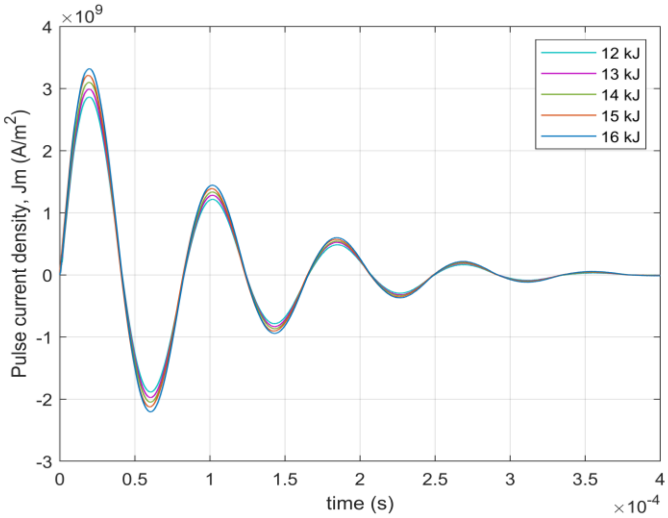

Figure 3: Pulsed current profile as a function of time

4.2.2 Numerical modelling

The transient electromagnetic analysis was conducted using a three-dimensional model consisting of the tube, the coil and the surrounding medium with 8-node electromagnetic element, as shown schematically in Figure 4(a). The mesh of the tube consists of 48000 elements; a tiny element of 10 µm thickness was used near the external surface to account for the skin effects. The coil was meshed with 11385 elements. The air medium – 125mm from the coil centre in the X direction and 154 mm in the Y direction was modelled and meshed with 203298 elements. Mirror asymmetric Dirichlet boundary condition was applied at the symmetry plane for the load current.

The tube and the backplate were modelled using an 8-node solid element (C3D8R) for the implicit dynamic analysis, seen in Figure 4(b). The identical mesh was adopted for the tube in the dynamic modal, while the backplate was meshed with 53568 elements. The interaction between the upper tube surface and the backplate was modelled using surface-to-surface contact. The classical Lagrange multiplier method of constraint enforcement was used for the normal behaviour, and a friction coefficient of 0.5 was adopted for the tangential behaviour. The separation between the tube and the backplate was allowed. The first three cycles of the pulsed current with a total duration of 250 µs were applied.

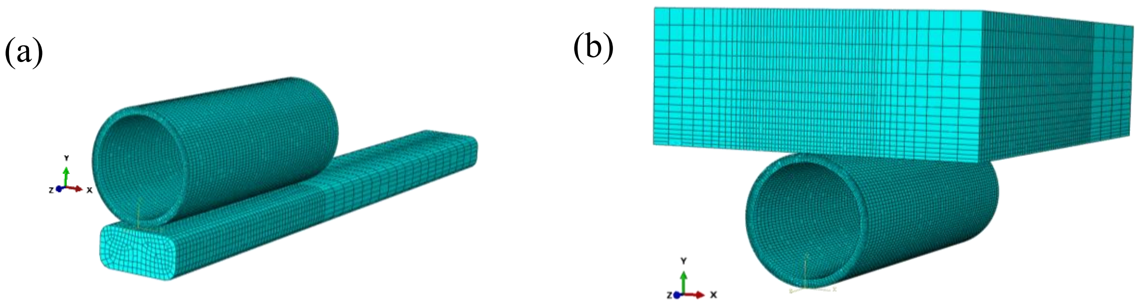

Figure 4:One-way coupled EM-Mechanical model for the tube compression experiment by EMPT based on (a) Electromagnetic model and (b) Dynamic model

4.2.3 Material model

The Johnson-Cook (JC) plasticity model was used to account for the hardening behaviour of the alloy 6063-T6 concerning the strain rate sensitivity. Expressed in Equation 13, the JC model is widely used to characterise the flow stress as a function of strain, strain rate and temperature. It consists of three terms, the first bracket is the elastic-plastic term, the second is the viscosity term, and the third is the thermal softening term.

$$\sigma = (A + B\epsilon^{n})(1 + C ln\dot{\epsilon}^{*})(1 - T^{*m}) \qquad \text{Equation 13}$$

where σ is the flow stress, ϵ is the plastic strain, $\dot{\epsilon}^{*}$ is the plastic strain rate ($\dot{\bar{\epsilon}}^{pl}$) normalised with respect to a reference strain rate ($\dot{\epsilon_0} = 1s^{-1}$), and $T^{*m} = (T - T_{ref})/(T_m - T_{ref})$, in which T_{ref} is the reference temperature, assumed to be 25 °C, T_m is the melting temperature of the alloy. The empirical constants are: A, the yield stress at reference temperature; B, the strain hardening modulus; C, the strain rate factor, n, the work hardening exponent and m, the thermal-softening exponent. The material properties of alloy 6063-T6 and the parameters of the JC model used in the simulation are summarised in Table 3.

Table 3: Material parameters of 6063-T6 used for finite element modelling

Parameters	Material
Electrical conductivity (S m)	29411765
Magnetic permeability (H m)	$1.26\text{x}10^{-6}$
Density (kg m)	2700
Specific heat (J kg K)	900
Thermal conductivity (W m K)	151
Coefficient of thermal expansion (K)	$2.32\text{x}10^{-5}$
Young's modulus (GPa)	72.4
Poisson's ratio	0.33
Johnson-Cook parameters:	
Melting temperature, Tm (°C)	650
Reference temperature, Tref (°C)	25
Thermal softening exponent, m	1
A (MPa)	190
B (MPa)	300
Strain hardening exponent, n	0.5
Strain-rate hardening coefficient, C	0.01

5 Results and discussion

5.1 Magnetic field attenuation in space

The magnetic flux density (EMB) in the workpiece attenuates as it is being accelerated away from the coil. This spatial attenuation was investigated using a series of EM simulations. The distance between the tube bottom point A and the coil, as shown in Figure 5, was 0.5 mm, 3 mm, 5.5 mm, 11 mm, 16 mm and 22 mm, respectively, in each model.

Figure 6 shows the simulated magnetic flux density distribution in each case. The spatial attenuation of B is clearly observed. This series of simulations revealed deterministically the spatial reduction of the induced emf that corresponds to the first term in Equation 11. Figure 7 plots the reduction ratios of the EMB at the bottom of the tube for each tube position. Exponential decay is observed in the relationship between the EMB and the distance. The ratio has a unity value when the tube bottom is initially placed 0.5 mm above the coil.

The eddy current (EMCD) generated in the tube is consequently reduced due to the EMB reduction, according to Equation 6. The reduction in both EMB and EMCD consequently decreases the Lorentz force, according to Equation 7. The reduction ratios of the EMCD and the Lorenz body force (EMBF) for each tube position are also included in Figure 7. The magnitude of EMB and EMCD is linearly proportional to the intensity of the coil current; hence they share the same reduction ratios, whereas the reduction ratio of EMBF is the square of that of the EMB/ EMCD, which is in line with Equation 7.

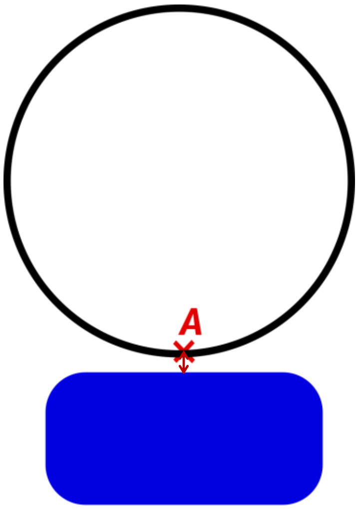

Figure 5: Schematic view of the distance between tube and coil

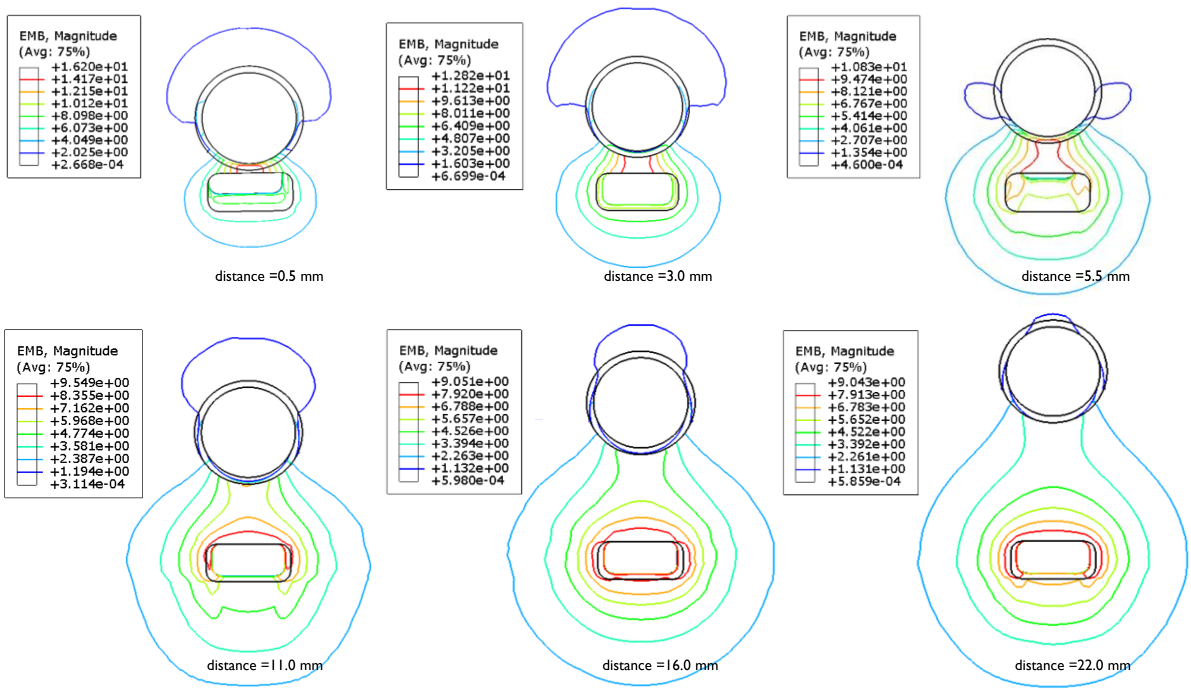

Figure 6: Magnetic flux density distribution with varying distance between tube and coil

The exponential decay relationship between the reduction ratio and the position in the magnetic flux density provides a map for determining the EMB reduction based on the displacement of the tube. As the displacement is a function of time, the reduction ratio of EMB also evolves as a function of time. The two timestamps of particular interest are the starting and ending point of the deformation. The velocity at the two points is zero, therefore there is no reduction effect of the motional emf. In other words, the reduction coefficient k has an initial value k_0=1.0, and its final value k_b equals the value of the EMB reduction ratio at the final position of the tube.

Figure 8 shows the deformed middle cross-section of the tube after being subjected to the pulse current with the discharging energy of 12kJ. The bottom surface is 12.31 mm above the coil. At this final displaced position, k_b =0.416 was estimated based on the EMB—distance relationship shown in Figure 7. Similarly, the value of k_b can be determined for the various energy levels based on their final deformation profile. The results are summarised in Table 4.

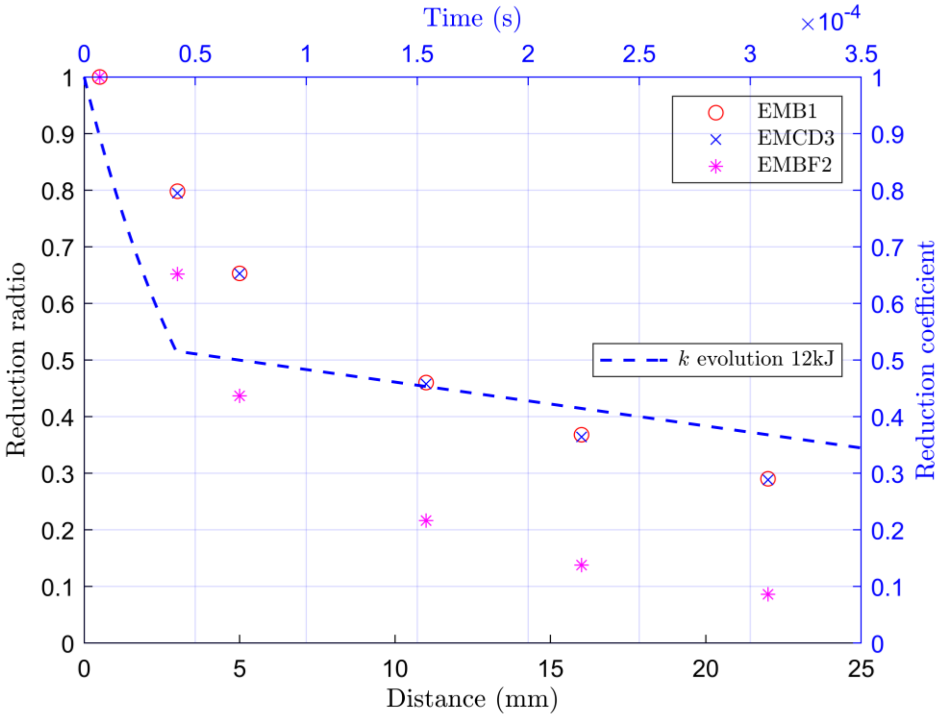

Figure 7: Reduction ratio of EMB, EMCD, EMBF; model k *evolution*

5.2 Reduction effect of velocity

Besides the spatial attenuation of the EMB, the other influencing factor in the reduction coefficient model *k* is the motional emf due to the velocity. One characteristic of the tube compression process is the zero velocity at the initial and end positions. Correspondingly, the reduction coefficient *k* starts as 1.0 from the initial position and finishes with k_b. The evolution of *k* between the two positions is affected by the development of the motional emf.

In order to quantify the impact of the motional emf, the velocity of the tube was investigated. An implicit dynamic analysis was carried out using the Lorenz body force resulted from the un-modified one-way coupled EM analysis. Figure 9(a) shows the evolution of the magnetic flux (EMB1) and the eddy current (EMCD3) at the tube bottom, sampled at point A in the FE model. The phase delay in the propagation of the magnetic field is observed. The Lorentz body force (EMBF2), the cross-product of the EMB1 and EMCD3 is plotted in Figure 9(b).

A change of direction is observed in the EMBF2 at the end of each wave, caused by the out-of-phase between the EMB1 and EMCD3. At the end of the first wave, the EMBF2 acts in the negative direction of Y, resulting in negative acceleration, shown in Figure 9(b). Since about 80% of the electrical energy is discharged after the first cycle (T_0 =82 µs), the acceleration starts to level off after two waves.

Figure 9(c) plots the velocity of the tube in the Y-direction during the first three cycles of the input coil current. The tube bottom reaches its maximum velocity at around 27 µs which is the first peak point of the coil current. The velocity starts to slow down as the acceleration turns negative at the end of the first half cycle and shows a small second jump during the second half of the first cycle. After that, it gradually drops to zero at the end of the deformation. The velocity history consists of the initial strong accelerating stage and the second gradual decay stage.

Since the motional emf is proportional to the velocity, its evolution follows the same progression to the velocity. It is reasonable to simplify the evolution of the motional emf into two stages: an accelerated growth to its maximum value in the first half cycle of the coil current; and a gradual decrease to zero. The motional emf generates the current that opposes the eddy current hence reduces the net current in the tube. This reduction effect quickly reaches its peak impact within the period of $\frac{T_0}{2}$, followed by a gradual decrease to zero.

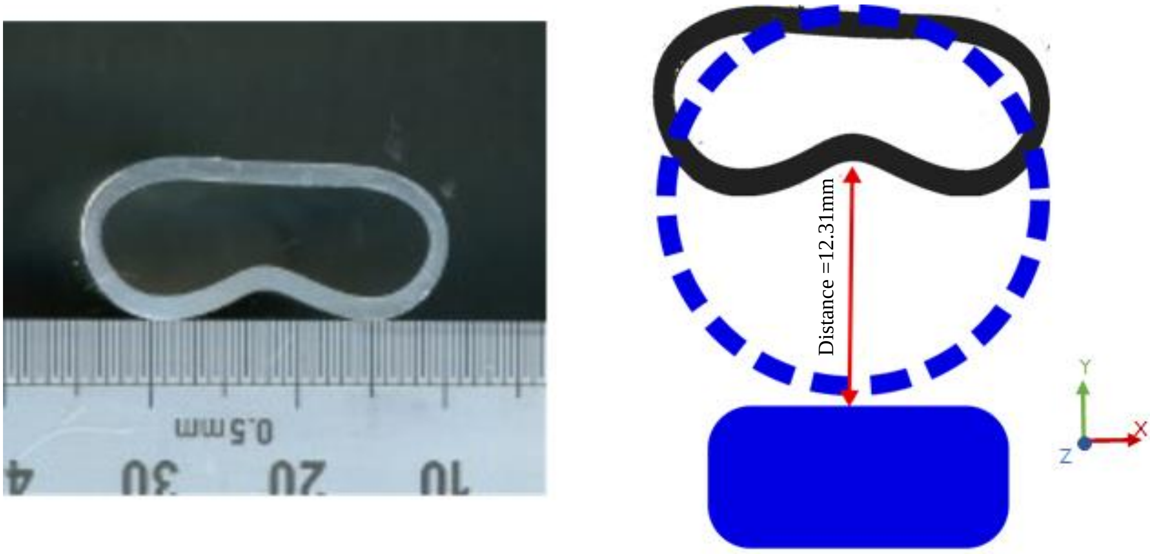

Figure 8: Mid-tube cross-section deformation, Discharging energy =12 kJ

Table 4: Spatial reduction of EMB *at the final position*

Discharge energy (kJ)	12	13	14	15	16
Distance (mm)	12.31	15.11	16.71	16.86	16.91
k_b	0.416	0.367	0.345	0.344	0.343

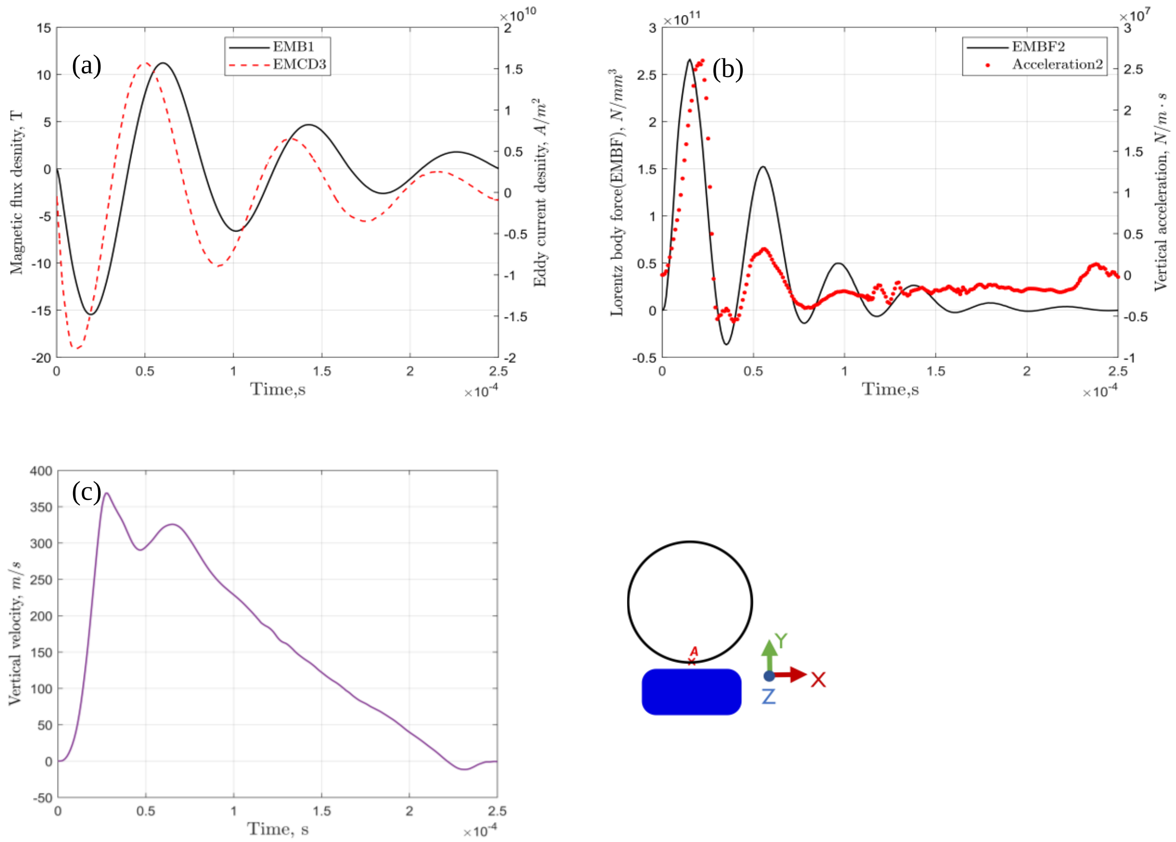

Figure 9: Simulation results at point A, during first three pulsed current cycles with a discharge energy of 12 kJ, showing (a) magnetic flux density in X direction and eddy current in Z direction, (b) Lorentz body force and acceleration in Y direction, first half input current cycle and (c) velocity of the tube in the Y-direction

5.3 Evolution function of the reduction coefficient model, k

The model *k* should encompass the evolution of the magnetic flux density and the velocity: the exponential decay relationship between the magnetic flux density and the distance between the tube and coil observed in Section 5.1; the two-staged velocity time history discovered in Section 5.2. Therefore the Equation 14 is proposed to represent the evolution of the reduction coefficient model. Within the first half cycle of the pulse, the *k* is approximated by an exponential decay function of time, and a linear function approximates the remaining.

$$k = \begin{cases} exp^{-\tau \cdot t}, & t \leq T_0/2 \\ \alpha t + \beta, & T/2 < t \end{cases} \qquad \text{Equation 14}$$

Equation 14 has an initial value of 1.0, satisfying the requirement of the initial value of *k*, k_0 =1.0, as discussed in Section 5.2. The function parameter τ captures the combined reduction effect of the magnetic flux density and the emotional emf, and is obtained through a trial-error process. The determined values provide the best-matched deformation profiles when compared with the experimental observations. The τ is the only parameter that is determined by the engineering judgment. Once the τ is determined, the other two parameters α and β can be subsequently calculated since the linear relationship goes through the point $(\frac{T_0}{2}, exp^{-\tau \cdot \frac{T_0}{2}})$ and the final point (t_p, k_b). The value k_b is based on the final position of the tube in the magnetic field and was determined using numerical simulation for different energy levels as summarised in Table 4. A typical evolution of *k* is depicted in Figure 7.

5.4 Calibration of the parameter τ

The parameter τ was obtained through a trial-error process, the determined values provide the best-matched deformation profiles when compared with the experimental observations. Table 5 summarises the exponential decay parameters determined for each pulse current. The maximum velocity in the workpiece obtained using the un-modified one-way coupled model, i.e., the one-way coupled electromagnetic-mechanical model without the model k implemented, are also included in the table. It's observed that a higher maximum velocity gives rise to a higher decay parameter. Based on the parameters determined for the five tested energy levels, a linear interpolation could be used to obtain the value of τ for a higher energy level.

Table 5: Exponential decay parameter τ

Input energy (kJ)	12	13	14	15	16
Max. velocity (m/s)	368	401	431	459	486
τ	16000	17500	18135	19100	20050

The accuracy of the modified one-way coupled model, i.e., the one-way coupled electromagnetic model with the model k implemented using the determined value of τ, was examined using a comparison study of the deformation profiles between the experimental data and the simulation results of the unmodified and modified models. Four dimensional parameters and two curvature ratios were compared, which are discussed in the following section.

5.4.1 Deformation profile comparisons

Figure 10a(i) Figure 12shows the dimensions of the deformed mid-section of the tube after subjected to the electropulse with input energy of 12 kJ. Figure 10a(ii) shows the simulated deformation shape using the un-modified one-way coupled electromagnetic-mechanical model. The curvature of the cross-section implies higher accelerations in the simulation than that in the experiment. High initial accelerations resulted in localised deformation quickly developed at the tube bottom while leaving the upper half of the tube under-deformed. The distance *d*, the final measured gap between the top and bottom of the tube surface, reached 4.8 mm at the early time step =51.2 μs. The subsequent excessive displacement in the un-modified model further signifies an overall higher acceleration in the unmodified model. Figure 10a(iii) shows the simulated deformation shape using the modified one-way coupled electromagnetic-mechanical model. Under the same distance d =4.8mm, a substantial improvement in the deformation profile was observed, with a notably increased accuracy of the predicted upper tube curvature. The upper tube curvature can be qualitatively assessed using the ratio $cuv1 = d/(x/2)$, and the bottom tube curvature can be assessed similarly using $cuv2 = h/(x/2)$.

In the case of 12kJ, compared with the measured results, the modified one-way model improved the prediction error from 15.7% to 2.0% for $cuv1$, 248.3% to 37.5% for $cuv2$. This improvement suggests that the accelerations in the modified model, especially the initial accelerations within the first half wave of the pulse, are in better agreement with the actual experimental experience.

The deformation profile comparison for input energy 13 kJ, 14 kJ, 15 kJ and 16 kJ are also included in Figure 10. As the input energy increases, the localised displacement of the tube bottom becomes more significant, which is understandably due to higher acceleration. What is interesting is that the observed upper tube curvature becomes flatter. The un-modified one-way model shows a consistent failure in predicting the curvature profile of the upper tube.

Meanwhile, the deformation profile predicted by the modified one-way model for all the tested input energies exhibits excellent agreement with the experimental observations.

Table 6 compares the dimensions of the deformed mid-tube cross-section between the experimental observation and the simulation results for the five input energy levels. An overall consistent improvement in the deformation profile was demonstrated. Table 7 presents the curvature ratios, *cuv1* and *cuv2*, calculated based on the experimental observations and simulation results. For the five energy levels, the modified one-way model reduced the mean approximation error of *cuv1* and *cuv*2 from 16.0 % to 1.0 %, 105% to 12%, respectively.

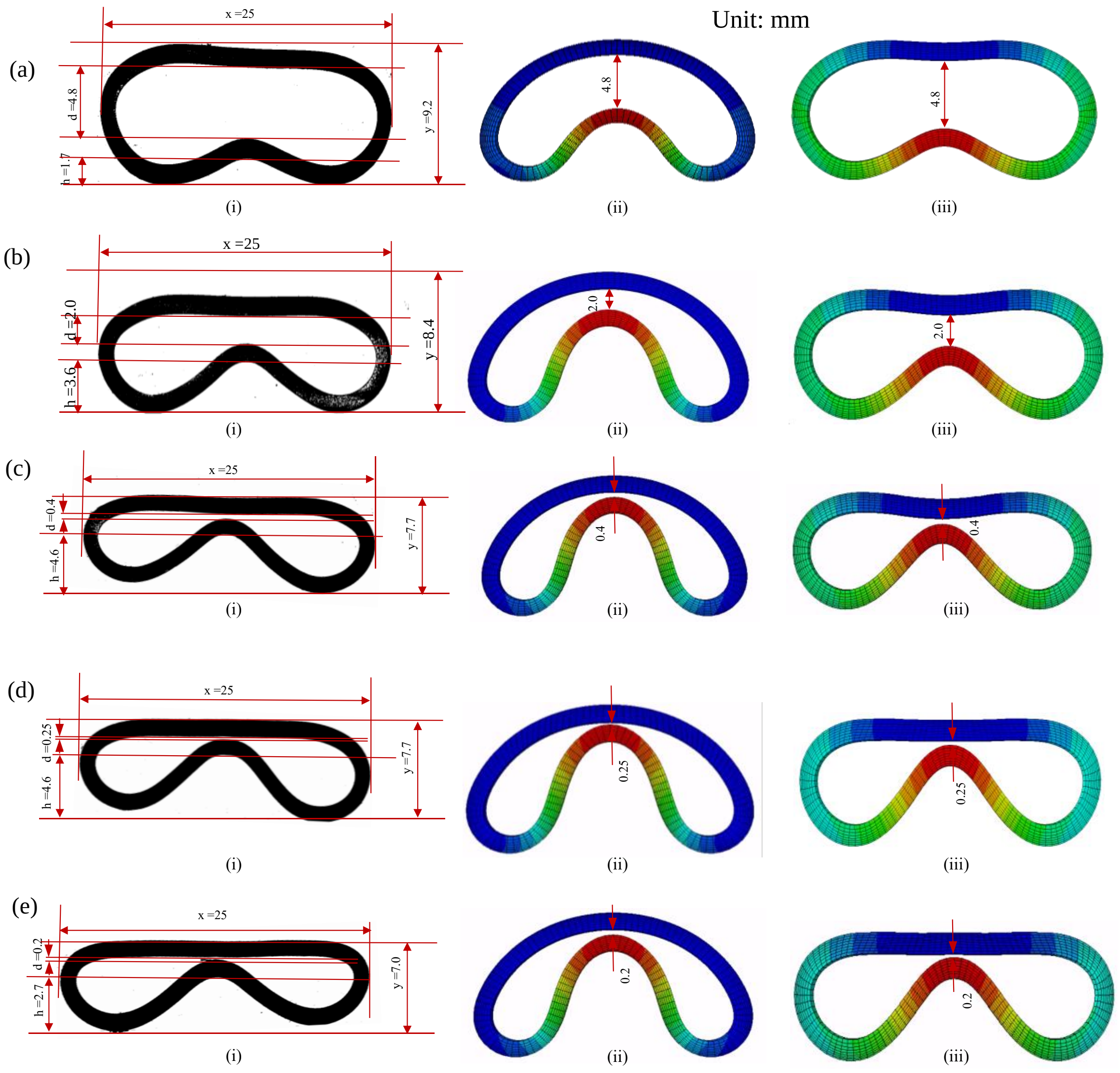

Figure 10: Deformed mid-tube cross-section by input energy (a) 12 kJ,(b) 13 kJ,(c) 14 kJ, (d) 15kJ and (e)16 kJ ,obtained from (i) experimental observations and computer simulation of deformation shape using the (ii) un-modified and (iii) modified one-way coupled electromagnetic-mechanical models.

Table 6: Deformed mid-tube cross-section dimensions with different input energies

Input energy (kJ)	**Dimensions (mm)**	**Experimental observations (mm)**	**One-way model without *k* (mm)**	**One-way model with *k* (mm)**
12	**d**	4.8	4.8	4.8
	h	1.7	5.1	2.3
	x	25.0	21.6	24.6
	y	11.00	12.4	9.8
13	**d**	2.0	2.0	2.0
	h	3.6	3.6	3.5
	x	25.0	20.6	24.8
	y	8.4	11.7	8.2
14	**d**	0.4	0.4	0.4
	h	4.6	7.8	4.3
	x	25.0	21.0	24.8
	y	7.7	10.6	7.5
15	**d**	0.25	0.25	0.25
	h	4.9	8.2	4.7
	x	25.0	20.6	24.6
	y	7.7	10.8	7.5
16	**d**	0.20	0.20	0.20
	h	3.9	8.3	4.7
	x	25.0	20.6	24.6
	y	7.0	10.8	7.6

Table 7: Curvature ratios at mid-tube cross-section obtained from experimental observations and simulation by one-way model w/o k

Energy (kJ)	**Curvature**		**Experimental observations**	**One-way model without *k***	**One-way model with *k***
12	*Cuv*1	Ratio	0.384	0.444	0.390
		Approx. Error (%)	-	15.7	1.6
	*Cuv*2	Ratio	0.136	0.474	0.187
		Approx. Error (%)	-	248.3	37.5
13	*Cuv*1	Ratio	0.160	0.194	0.161
		Approx. Error (%)	-	21.4	0.8
	*Cuv*2	Ratio	0.288	1.320	0.282
		Approx. Error (%)	-	358.5	2.0
14	*Cuv*1	Ratio	0.032	0.038	0.032
		Approx. Error (%)	-	19.0	0.8
	*Cuv*2	Ratio	0.368	0.743	0.347
		Approx. Error (%)	-	101.9	5.8
15	*Cuv*1	Ratio	0.020	0.024	0.020
		Approx. Error (%)	-	21.4	1.6
	*Cuv*2	Ratio	0.392	0.796	0.382
		Approx. Error (%)	-	103.1	2.5
16	*Cuv*1	Ratio	0.016	0.019	0.016
		Approx. Error (%)	-	21.4	1.6
	*Cuv*2	Ratio	0.312	0.806	0.382
		Approx. Error (%)	-	158.3	22.5
All	*Cuv*1	Mean Approx. Error (%)	-	16	1
	Cuv2	Mean Approx. Error (%)	-	105	12

A further comparison study was performed for better understanding the influence of the magnetic field distribution. In this separate analysis, the reduction ratio of k_b, the magnetic flux density at the final position of the tube, was applied to the input current in the numerical model. The simulated deformation profile are presented in Figure 11 for the input energy 12 kJ and 16 kJ respectively. Compared to the experimental observation, the deformation profiles seen in Figure 11 show substantial underestimation. This comparison results highlight the time-dependence nature of the magnetic field reduction effect. The evolution of the reduction effect has to be properly represented at every time point by the model *k* in order to accurately simulate the deformation of the tube.

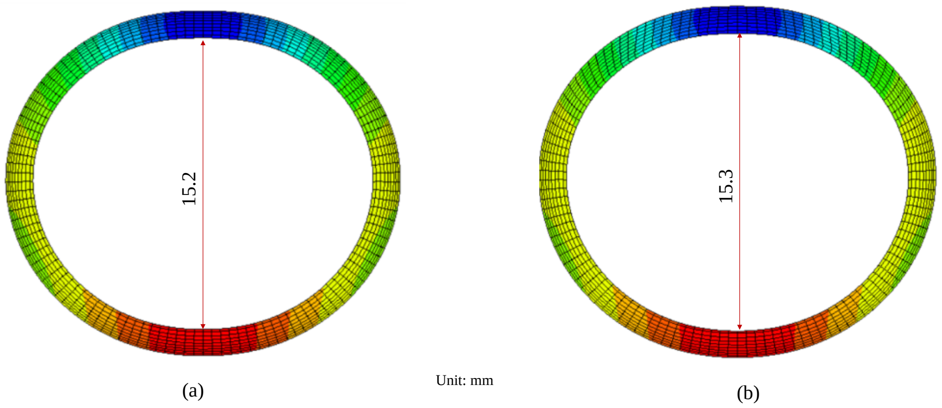

Figure 11: Simulated deformation shape using the input current reduced by a single factor kb (a) kb =0.416, Input energy 12 kJ (b)) kb =0.343, Input energy 16 kJ

5.5 Sensitivity to material properties

The reliability of FEM simulations is based on the accuracy of the deformation behaviour described by the constitutive material model. The Johnson-Cook (JC) model was adopted to account for the high strain rate in the EMPT process. The simulation used three different values of the strain rate parameter C to study its influence on the deformation behaviour. The predicted tube bottom displacements were compared. Figure 12 shows that the deformation results exhibit a strong sensitivity to the strain rate parameter. This observation suggests that EMPT is a highly dynamic process. In this EMPF, the deformation rate of the tube experiment is so high that the plastic flow in the material is no longer dominated by the dislocation motion but viscous phonon drag [24]. Table 8 summarises the maximum strain rate at three different positions within the midspan cross-section, illustrated in Figure 13.

The tube bottom, point A, experiences the highest strain rate, corresponding to the largest localised deformation at the bottom of the tube. The maximum strain rate experienced under input energy of 12 kJ is 8.2×10^3 s^{-1} and is 10.2×10^3 s^{-1} under 16 kJ. It has been reported that for aluminium alloys, the flow stress increases more rapidly when the strain rate starts exceeding 10^4 s^{-1} [25]. Consequently, a different strain rate sensitivity parameter C in the Johnson-Cook model should be considered for regions with high strain rates in the material. A preliminary study was carried out to investigate the impact of parameter C on the predictions of the deformation profile. For the case of 16 kJ, a value of 0.25 was adopted for C in the material model for the region around position A depicted in Figure 13. Table 9 compares the curvature ratios determined using the two different strain rate sensitivity parameters. By allowing a stronger strain rate dependency at the bottom region, the accuracy of the predicted ratios was further improved, with the approximation error of cuv1 and cuv2 reduced to 0.4 % and 10.7%, respectively, from 1.6% and 22.5%.

It is noted that a distinctive strain rate variation within the cross-section could be obtained using one electropulsing treatment because the magnetic pressure concentrates at the bottom region while the rest of the tube moves out of inertia. This characteristic of the tube compression test suggests it could be used to test materials under dynamic deformation. By modifying the strain rate sensitivity parameter C at different positions to refine the matching of the deformation profile, the material's stress-strain curves under different strain rates could be calibrated. It has been seen over the years that some materials behave differently under EMF from the quasi-static forming [16]. The tube compression test combined with FE simulation presents a potential method to determine the dynamic mechanical stress strain behaviours of alloys efficiently.

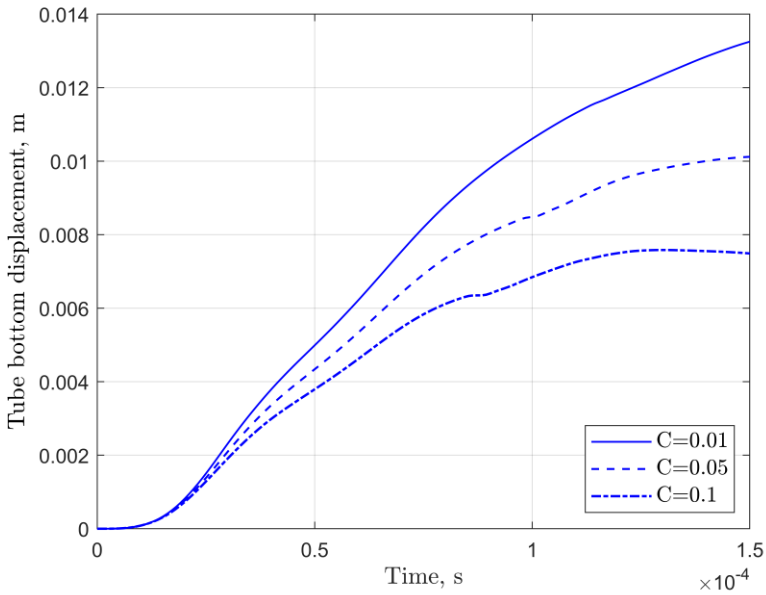

Figure 12: Tube bottom displacement at mid-section with varying strain-rate factor C, input energy=12 kJ

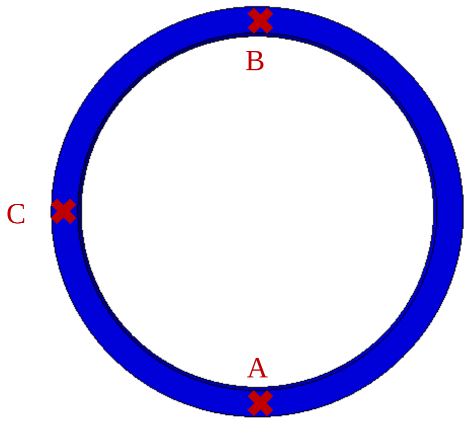

Figure 13: Strain rate positions sampled at mid-section

Table 8: Strain rate distribution within mid cross section

Input energy (kJ)	Position	Max. Strain rate (s^{-1})
12	A	8.2 x10^3
	B	3.1 x10^3
	C	3.1 x10^3
16	A	10.2 x10^3
	B	3.7 x10^3
	C	3.8 x10^3

Table 9: Curvature ratios at mid-tube cross-section with different strain rate sensitivity parameter

	d	**h**	**x**	**y**	**Ratio, *cuv1***	**Approx. Error (%)**	**Ratio, *cuv2***	**Approx. Error (%)**
Experimental observations	0.20	3.9	25.0	7.0	0.0160	-	0.3120	-
One-way model with *k*, c =0.01	0.20	4.7	24.6	7.6	0.0163	1.6%	0.3821	22.5%
One-way model with *k*, c=0.01 combined with bottom area c =0.025;	0.20	4.3	24.9	7.2	0.0161	0.4%	0.3454	10.7%

Figure 14 presents a flowchart showing the accelerated one-way coupled electromagnetic-mechanical model with the reduction coefficient model k incorporated. As a first step, a calibration of the k using the tube compression tests following the process described in Section 5 should be carried out for a specific tool coil to enable the implementation of the accelerated model. For any specific EMF/EMPW process, the value of k_b of the workpiece can be determined based on the magnetic field attenuation map obtained through the series of electromagnetic analyses in the calibration process since the final position of the workpiece is generally decided by the spacing between the workpiece and the target plate or mandrel. The maximum velocity in the workpiece found by the un-modified one-way coupled electromagnetic-mechanical analysis is used to assist the determination of the parameter τ using linear interpolation refereeing to the values of τ obtained during the calibration process based on the deformation profile comparison, for example, the τ values summarised in Table 5. Once the τ is determined, the other two parameters α and β in Equation 14 can be calculated with two known points on the linear relationship $(\frac{T_0}{2}, exp^{-\tau\cdot\frac{T_0}{2}})$ and (t_p, k_b). The obtained model k is subsequently applied to the coil current input to establish the modified one-way coupled electromagnetic-mechanical model.

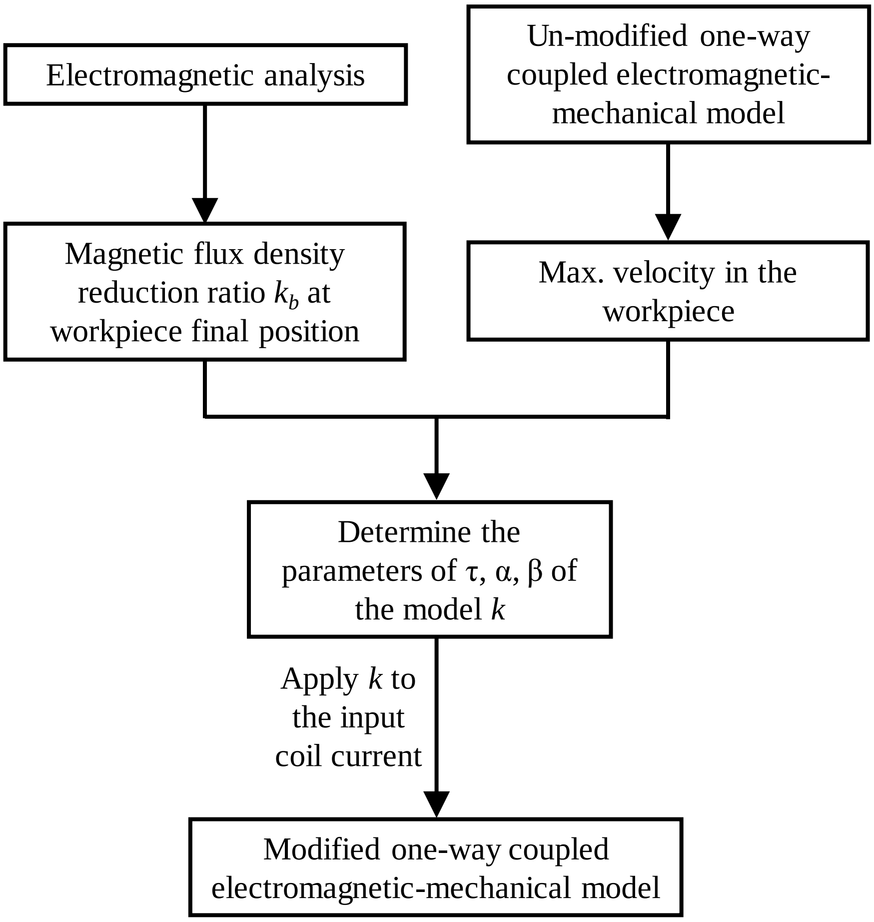

Figure 14: Flow chart of the accelerated one-way coupled electromagnetic-mechanical model

6 Conclusions

A modified three-dimensional one-way coupled electromagnetic-mechanical model was established in Abaqus to accelerate the numerical analysis of the electromagnetic forming and welding process.

The modification –incorporating a reduction coefficient model *k* into pulse loading enables the one-way coupled model to account for the magnetic field attenuation and the motional emf experienced by the workpiece during the electropulsing process. Being constructed as a function of time, the model *k(t)* is directly applied to the input loading history, allowing both the spatial and temporal reduction of the magnetic field in the workpiece to be properly simulated at every time point of the process. The coefficient model was calibrated and validated by a series of Al tube compression tests combined with numerical simulations. The model is proven to efficiently and adequately assess the electromagnetic field distribution while reducing the computational burden otherwise required by a fully coupled three-dimensional electromagnetic-mechanical analysis. The accelerated three-dimensional one-way coupled electromagnetic-mechanical model offers valuable assistance in better understanding, designing and optimising the EMF/EMPW process parameters.

The sensitivity study of the strain rate parameter C in the Johnson-Cook material model demonstrated that electropulsing treatment is a highly dynamic process and highlighted its potential application in dynamic material testing.

Table 10: List of symbols

Symbol	Meaning	Symbol	Meaning
emf	Electromotive force	γ	material electrical conductivity
$\boldsymbol{E}_{ind}$	Induced electric field	μ	magnetic permeability
$\boldsymbol{B}$	Magnetic flux density	μ_0	magnetic permeability
$\boldsymbol{E}$	Electric field intensity	ϵ	electrical permittivity
$\boldsymbol{J}_{tot}$	Total current density	ϵ_0	electrical permittivity of vacuum
$\boldsymbol{J}_{con}$	Conduction current	σ	Flow stress
ρ_{tot}	Total charge density	ϵ	Plastic strain
r	position vector	$\dot{\bar{\epsilon}}^{pl}$	Plastic strain rate
$\boldsymbol{v}$	Velocity vector	τ, α, β	Reduction coefficient model equation parameters
k	Reduction coefficient model	T_0	Cycle period of coil current
k_b	Value of k at final position	t_p	Period duration of the coil
d,h,x,y	Dimensions of the deformed tube	*cuv1*	$cuv1 = d/(x/2)$
EM	Electromagnetic	*cuv2*	$cuv2 = h/(x/2)$
EMB	Magnetic flux density	EMPT	Electromagnetic pulse technology
EMCD	Eddy current density	EMPF/EMF	Electromagnetic pulse forming
EMBF	Lorentz body force	EMPW	Electromagnetic pulse welding

Acknowledgements

The authors thankfully acknowledge financial support from Innovate UK under project 104324: Aluminium for Ultra Low Emission Vehicles (Al-ULEV). This study is also grateful for the financial support of the EPSRC Future Electrical Machines Manufacturing (FEMM) Hub, Subject No. R/155683.

References

[1] Schäfer R, Pasquale P, Kallee S. Industrial application of the electromagnetic pulse technology. PST Prod Gmbh, Alzenau, Ger 2009.

[2] Li Z, Beslin E, den Bakker AJ, Scamans G, Danaie M, Williams CA, et al. Bonding and microstructure evolution in electromagnetic pulse welding of hardenable Al alloys. J Mater Process Technol 2021;290. https://doi.org/10.1016/j.jmatprotec.2020.116965.

[3] Chen S, Jiang X. Microstructure evolution during magnetic pulse welding of dissimilar aluminium and magnesium alloys. J Manuf Process 2015;19:14–21. https://doi.org/10.1016/j.jmapro.2015.04.001.

[4] Pereira D, Oliveira JP, Santos TG, Miranda RM, Lourenço F, Gumpinger J, et al.

Aluminium to carbon fibre reinforced polymer tubes joints produced by magnetic pulse welding. Compos Struct 2019;230:111512.

[5] Iriondo E, Gutiérrez MA, González B, Alcaraz JL, Daehn GS. Electromagnetic impulse calibration of high strength sheet metal structures. J Mater Process Technol 2011;211:909–15.

[6] Sapanathan T, Raoelison RN, Buiron N, Rachik M. Magnetic pulse welding: an innovative joining technology for similar and dissimilar metal pairs. Join. Technol., InTech; 2016, p. 243–73.

[7] Cai W, Daehn G, Vivek A, Li J, Khan H, Mishra RS, et al. A state-of-the-art review on solid-state metal joining. J Manuf Sci Eng Trans ASME 2019;141:1–35. https://doi.org/10.1115/1.4041182.

[8] Hokrai, H. Sato T, Kawauchi K, Muto A. Magnetic impulse welding of aluminium tube and copper tube with various core materials. Weld Int 1998;12:619–26. https://doi.org/10.1080/09507119809452024.

[9] Yu H, Dang H, Qiu Y. Interfacial microstructure of stainless steel/aluminum alloy tube lap joints fabricated via magnetic pulse welding. J Mater Process Technol 2017;250:297–303. https://doi.org/10.1016/j.jmatprotec.2017.07.027.

[10] Shanthala K, Sreenivasa TN, Choudhury H, Dond S, Sharma A. Analytical, numerical and experimental study on joining of aluminium tube to dissimilar steel rods by electro magnetic pulse force. J Mech Sci Technol 2018;32:1725–32. https://doi.org/10.1007/s12206-018-0328-0.

[11] Bellmann J, Schettler S, Dittrich S, Lueg-Althoff J, Schulze S, Hahn M, et al. Experimental study on the magnetic pulse welding process of large aluminum tubes on steel rods. IOP Conf Ser Mater Sci Eng 2019;480. https://doi.org/10.1088/1757-899X/480/1/012033.

[12] Shotri R, Faes K, De A. Magnetic pulse welding of copper to steel tubes–Experimental investigation and process modelling. J Manuf Process 2020;58:249–58. https://doi.org/10.1016/j.jmapro.2020.07.061.

[13] Marya M, Marya S. Interfacial microstructures and temperatures in aluminium–copper electromagnetic pulse welds. Sci Technol Weld Join 2004;9:541–7. https://doi.org/10.1179/174329304X8685.

[14] Kore SD, Imbert J, Worswick MJ, Zhou Y. Electromagnetic impact welding of Mg to Al sheets. Sci Technol Weld Join 2009;14:549–53.

[15] Luca D. A numerical modelling: opened perspectives to increase the performance of the electromagnetic forming processes. Int J Numer Model Electron Networks, Devices Fields 2012;25:15–23.

[16] Psyk V, Risch D, Kinsey BL, Tekkaya AE, Kleiner M. Electromagnetic forming - A review. J Mater Process Technol 2011;211:787–829. https://doi.org/10.1016/j.jmatprotec.2010.12.012.

[17] Qiu L, Xiao Y, Deng C, Li Z, Xu Y, Li Z, et al. Electromagnetic-structural analysis and improved loose coupling method in electromagnetic forming process. Int J Adv Manuf Technol 2017;89:701–10. https://doi.org/10.1007/s00170-016-9071-9.

[18] Paese E, Geier M, Homrich RP, Rosa P, Rossi R. Sheet metal electromagnetic forming

using a fl at spiral coil : Experiments , modeling , and validation. J Mater Process Tech 2019;263:408–22. https://doi.org/10.1016/j.jmatprotec.2018.08.033.

[19] Oliveira DA, Worswick MJ, Finn M, Newman D. Electromagnetic forming of aluminum alloy sheet : Free-form and cavity fill experiments and model 2005;170:350–62. https://doi.org/10.1016/j.jmatprotec.2005.04.118.

[20] Haiping YU, Chunfeng LI, Jianghua DENG. Sequential coupling simulation for electromagnetic – mechanical tube compression by finite element analysis 2008;9:707–13. https://doi.org/10.1016/j.jmatprotec.2008.02.061.

[21] Uhlmann E, Prasol L, Ziefle A. Potentials of pulse magnetic forming and joining 2014;907:349–64. https://doi.org/10.4028/www.scientific.net/AMR.907.349.

[22] Eplattenier PL, Cook G, Ashcraft C, Burger M, Imbert J, Worswick M. Introduction of an Electromagnetism Module in LS-DYNA for Coupled Mechanical-Thermal-Electromagnetic Simulations 2009:351–8. https://doi.org/10.2374/SRI08SP152.

[23] Cao Q, Li L, Lai Z. Dynamic analysis of electromagnetic sheet metal forming process using finite element method 2014:361–8. https://doi.org/10.1007/s00170-014-5939-8.

[24] Kumar A, Kumble RG. Viscous drag on dislocations at high strain rates in copper. J Appl Phys 1969;40:3475–80. https://doi.org/10.1063/1.1658222.

[25] Troitskii OA. Pressure shaping by the application of a high energy. Mater Sci Eng 1985;75:37–50. https://doi.org/10.1016/0025-5416(85)90176-4.

[26] Zhang Y, Babu SS, Daehn GS. Interfacial ultrafine-grained structures on aluminum alloy 6061 joint and copper alloy 110 joint fabricated by magnetic pulse welding. J Mater Sci 2010;45:4645–51. https://doi.org/10.1007/s10853-010-4676-0.